Science and Technology of Advanced Materials

ISSN: 1468-6996 (Print) 1878-5514 (Online) Journal homepage: www.tandfonline.com/journals/tsta20

Time-domain thermoreflectance technique using multiple delayed probe pulses for high-throughput data acquisition and analysis

Hiroto Arima, Yuichiro Yamashita & Takashi Yagi

To cite this article: Hiroto Arima, Yuichiro Yamashita & Takashi Yagi (26 Jun 2025): Time-domain thermoreflectance technique using multiple delayed probe pulses for high-throughput data acquisition and analysis, Science and Technology of Advanced Materials, DOI: 10.1080/14686996.2025.2523240

To link to this article: https://doi.org/10.1080/14686996.2025.2523240

Publisher: Taylor & Francis & The Author(s). Published by National Institute for Materials Science inpartnership with Taylor & Francis Group.
Journal: *Science and Technology of Advanced Materials*
DOI: 10.1080/14686996.2025.2523240

Time-domain thermoreflectance technique using multiple delayed probe pulses for high-throughput data acquisition and analysis

Hiroto Arima, Yuichiro Yamashita, Takashi Yagi*
National Metrology Institute of Japan (NMIJ), National Institute of Advanced Industrial Science and Technology (AIST), Tsukuba, Ibaraki 305-8565, Japan

Corresponding author: t-yagi@aist.go.jp (Takashi Yagi)

Keywords: time-domain thermoreflectance, multiple delay, thin film, thermal effusivity, interfacial thermal resistance, machine learning

Abstract

To advance thermal control technology, improve thermal reuse efficiency, and further enhance device performance, it is crucial to understand microscopic spatial and temporal heat transport in materials. In this study, we developed a high-throughput time-domain thermoreflectance (HT-TDTR) technique that accelerates the measurement speed of thermophysical properties. The fundamental concept involves decomposing supercontinuum light into a pump pulse (1064 nm) and multiple delayed probe pulses (900 nm–730 nm) with different delays, enabling simultaneous acquisition of thermoreflectance signals at multiple delay times. Quartz glass, $SrTiO_3$ (100) single crystal, and c-plane sapphire were heated with picosecond pulsed light, and the temporal temperature decrease at six delay times was simultaneously measured. The thermal effusivities analyzed based on heat diffusion equation were consistent with the literature values. Furthermore, we applied machine learning-based analysis and demonstrated the ability to determine thermophysical properties from measurement data consisting of only a few delay points. With sufficient signal strength, machine learning can predict a reasonable thermal effusivity based on experimental data obtained in less than a second. HT-TDTR enables rapid and accurate measurement of samples based on information about thermal relaxation dynamics, facilitating more efficient characterization of thermophysical properties.

1. Introduction

To advance heat control technologies, improve heat reuse efficiency, and further enhance device performance, it is crucial to understand microscopic spatial and temporal thermal transport rather than relying solely on the macroscopic and static thermophysical properties of bulk materials. Recently, a combination of spintronics and thermal effects called "spin caloritronics" [1] has been attracting attention because the interconversion of spin, heat, and electric currents will lead to a thermal energy manipulation technology and an alternative approach to energy harvesting. To explore spin caloritronic materials, fast and accurate thermophysical property measurement techniques suitable for evaluating the dynamics and spatial distribution of thermophysical properties are important. For example, the giant magnetothermal resistance effect has been reported in ferromagnetic/paramagnetic metal ($Cu/Co_{50}Fe_{50}$) multilayers; however, high-speed measurements are required to investigate heat transport in magnetic fields in greater detail [2]. Additionally, in Sm-Co amorphous thin film prepared using the combinatorial sputtering method, high-throughput material evaluation revealed that $Sm_{20}Co_{80}$ exhibits temperature modulation induced by the anomalous Ettingshausen effect (AEE). The AEE occurs when current is applied to a magnetic material, generating heat flow in the direction perpendicular to both the current and magnetization. To further elucidate the detailed thermophysical properties of gradient-composition films grown using the combinatorial sputtering method, it is essential to investigate the spatial distribution of the thermophysical properties [3].

Time-domain thermoreflectance (TDTR) is widely used for measuring thermophysical properties such as thermal conductivity, thermal effusivity, and thermal diffusivity of thin films [4–6]; temporal temperature is measured based on the reflectance changes related to the temperature (TR) of a sample that is coated with a metal transducer. The TDTR technique monitors the TR signal as a function of the delay time between the pump and probe pulses, with a single delay sweep spanning a few nanoseconds. Because the acceleration of TDTR measurements allows for dynamic time-dependent analysis and mapping of thermophysical property distributions, great efforts have been made to improve the measurement speed of TDTR [7–9]. For example, Huxtable et al. have conducted thermal conductivity mapping using TDTR for a diffusion multiple comprising Nb-Ti-Cr-Si samples with a lateral spatial resolution of 3.4 μm. They acquired the thermal conductivity distribution of 100 × 100 pixels in approximately 1 h. In their measurements, thermal conductivity was estimated from the TR signal at a fixed delay time of 100 ps [7]. This delay time was chosen because the influence of the interface thermal conductance at the transducer-sample interface and the thermal diffusivity

of the transducer on the TR signal were small. The thermal conductivity was derived from the thermal effusivity under the assumption that the specific heat capacity of all samples remained constant. This thermal conductivity mapping technique requires prior measurement of the thermophysical properties of the sample. In Li_xCoO_2, the time-dependent variation in thermal conductivity due to lithiation and delithiation under an electric field was measured using TDTR [9]. During this measurement, the thermal conductivity was recorded every 6 s with a fixed delay time of 30 ps. To determine the real-time thermal conductivity during the electrochemical cycling, the complete TDTR data sets were corrected for the lithiated and delithiated states before the measurement. Using this method, the thermal conductivity of Li_xCoO_2 can be tuned between 5.4 W/(m K) (in lithiation) and 3.7 W/(m K) (in delithiation), providing insight into the thermal response to electric field control. These examples demonstrate that highly sensitive TDTR techniques can be used for high-throughput measurements. However, its application to samples, whose thermophysical properties cannot be predicted in advance, remains a challenge because the measured curves of the reference samples are required as a guide to derive the thermophysical properties from fixed-delay data.

Frequency-domain thermoreflectance (FDTR), which uses periodically modulated pump laser, is also often used for spatial distribution measurements of thermophysical properties in micro-scales [10, 11]. FDTR offers several advantages over TDTR, such as no mechanical delay stage and the use of inexpensive continuous-wave (CW) laser sources, making its implementation more accessible. However, to obtain information on the temporal dynamics of thermal relaxation in FDTR, a sufficient frequency range must be swept, leading to a certain amount of measurement time. Because a single fixed frequency is typically used for spatial distribution measurements in FDTR [12], the total data quality is expected to be similar to that of fixed-delay time TDTR.

TDTR and FDTR are powerful experimental techniques that are used to evaluate the thermophysical properties of thin films. However, slow data acquisition limits the measurement of temporal and spatial dynamics of materials. In previous approaches, the measurement speed was accelerated by fixing the delay time (in TDTR) or frequency (in FDTR) to a single point; however, this approach lacks information about the thermal relaxation dynamics of the samples. In this study, we introduce a high-throughput TDTR (HT-TDTR) technique that enables acceleration of the measurement speed while maintaining time-domain data. HT-TDTR utilizes a supercontinuum light source with a broad wavelength range from visible to infrared. The basic concept involves resolving the supercontinuum light into a pump pulse and multiple probe pulses with different delays, thereby allowing the TR signal for multiple delays to be acquired simultaneously. In addition, machine learning based analysis supports to find thermophysical properties from the data consisting of a small number of delay point. HT-TDTR can measure the

thermophysical properties quickly and accurately, preserving critical information on thermal relaxation dynamics.

2. High-throughput time-domain thermoreflectance apparatus

2.1 Overview of the apparatus

Figure 1 shows an overview of the HT-TDTR system. The light source for HT-TDTR is a supercontinuum laser (NKT Photonics FIU-15) that emits pulsed light with a broadband wavelength ranging from 350 nm in the visible spectrum to 2400 nm in the infrared spectrum, with a maximum power of 5.5 W. The supercontinuum spectrum is excited using a laser source with a wavelength of 1064 nm, a pulse duration of 6 ps, and a repetition rate of 78 MHz. The emitted pulsed light is processed through four main optical subsystems: a wavelength splitter, wavelength combiner, focusing optics, and thermoreflectance detection system to measure the thermoreflectance signals of the sample. Details of each subsystem are provided in the following sections. The supercontinuum beam is introduced into the wavelength splitter, where the broadband spectrum is split into a pump beam with a wavelength of 1064 nm and six probe beams with wavelengths ranging from 900 nm to 730 nm using multiple dichroic mirrors. The probe beams are coupled with optical fibers of different lengths to set certain delay times. The beams are then recombined into an optical fiber using a wavelength combiner. On the other hand, the pump beam is modulated at 780 kHz using an acousto-optic modulator (AOM) and the modulated pump beam is amplified in power by an ytterbium-doped fiber amplifier (YbFA). The pump and unified probe beams are directed to a focusing optical system, where all the beams are co-aligned coaxially and irradiate on the sample. The reflected probe beams are subsequently routed to a thermoreflectance detection system, where the beams are spectrally separated again and detected using photodiodes. The phase component of the thermoreflectance signals corresponding to each delay time are measured using multiple lock-in amplifiers. Finally, the phase signals of the thermoreflectance at six different delay times are obtained and analyzed using a machine learning database to identify the thermophysical properties of the samples. This process enables determination of the thermophysical properties of a sample.

2.2 Wavelength Splitter

Figure 2(a) illustrates the optical system of the wavelength splitter. The supercontinuum laser beam first reaches a short-pass dichroic mirror (SDM) with a cut-on wavelength of 1000 nm. A pump beam with a center wavelength of 1064 nm is extracted from the reflected beam using a bandpass (BP) filter. The transmitted beam with a wavelength below 1000 nm is subsequently split using long-pass dichroic mirrors (LDMs) from the longest wavelength of 900 nm to the shortest wavelength of 730 nm to provide six probe beams. These beams are extracted

with specific wavelengths of 900 nm, 850 nm, 830 nm, 815 nm, 790 nm, and 730 nm using BP filters with a bandwidth of 10 nm and coupled to each multi-mode optical fiber (core diameter of 25 μm, numerical aperture of 0.1) with lengths from 0.7 m to 2.7 m. The probe beams travel through the optical fibers and are directed into the wavelength combiner (see section 2.3). Pulse width of the supercontinuum laser broadens with the wavelength, resulting in a pulse width of approximately 30 ps over a 10 nm bandwidth. Figure 2(b) shows the spectrum of the SDM, LDMs, pump beam, and six probe beams observed using a spectrometer. The probe beams at 900 nm, 850 nm, 830 nm, 815 nm, 790 nm, and 730 nm were split with a wavelength bandwidth of 10 nm. The wavelengths of these probes were selected based on the thermoreflectance coefficient of the metal transducer film. We used a Mo film as a transducer, which exhibits positive thermoreflectance coefficients between 1.2 eV and 2.3 eV [13]. The highest coefficient was obtained at 1.4 eV, which corresponds to approximately 880 nm.

For the pump beam, the beam intensity was rectangularly modulated using an acoustic optical modulator (AOM) with a frequency of 780 kHz. After passing through the AOM, the pump beam was coupled to a single-mode optical fiber. The power of the pump beam was then increased using a YbFA before being introduced into the focusing optics (see section 2.4).

2.3 Wavelength Combiner

Figure 3(a) shows an overview of the wavelength combiner used to unify the probe beams with different delays. Each probe beam from the wavelength splitter travels through a different length of optical fibers and is then coupled into a multi-mode fiber (core diameter of 25 μm, numerical aperture, NA of 0.1). Figure 3(b) shows the temporal relationship between the pump and multiple probe pulses at the sample position observed using a high-speed photodiode (Newfocus 1444, 20 GHz) and an oscilloscope (Tektronix TDS8200, 20 GHz). The delay times of the probe pulses relative to the pump pulse are -120 ps for 900 nm, 150 ps for 850 nm, 523 ps for 830 nm, 1146 ps for 815 nm, 4673 ps for 790 nm, and 9969 ps for 730 nm. The 900 nm probe pulse is also used with a delay time of 12424 ps.

These delay times were designed based on a sensitivity analysis. The sensitivity S_ξ is calculated using the following equation:

$$S_\xi = \frac{\partial \ln \theta}{\partial \ln \xi} = \frac{\xi}{\theta}\frac{\partial \theta}{\partial \xi} \quad (1),$$

where ξ represents a specific parameter. Figure 4 shows the sensitivities for the lock-in phase of thermoreflectance for the transducer/substrate samples. Three thermal effusivities were tested for the substrate: 1000 J/(m^2 s$^{0.5}$ K), 5000 J/(m^2 s$^{0.5}$ K), and 10000 J/(m^2 s$^{0.5}$ K). In the graph, the thermal conductivity of a 100 nm-thick Mo transducer (K_{Mo}), the interfacial thermal resistance between the Mo and substrates (R), and the thermal effusivity (e) of the substrates are plotted.

The interfacial thermal resistance R exhibited almost no sensitivity for any of the samples. The sensitivity of e becomes higher as e decreases. The sensitivity peaks shifted from approximately 200 ps to 1000 ps when e increased. For K_{Mo}, higher sensitivity was obtained at approximately 100 ps. However, because other processes besides pure thermal relaxation may occur immediately after the pump pulse irradiation, the delay was set over 100 ps. We set three delay times shorter than 1200 ps, and the subsequent delays consisted of three delay times spaced nanoseconds apart. These six delay times can cover almost the entire range of the pulse repetition period of 12.8 ns (78 MHz of the pulse frequency).

2.4 Focusing Optics and Detecting System

The combined six probe beams and the modulated and amplified pump beam irradiate the samples using focusing optics, as shown in Fig. 5. The pump beam and the probe beams are coaxially combined by a dichroic mirror and focused on a sample with spot diameters of 25 μm using an objective lens with a power of 10 (Mitsutoyo, Plan APO IR ×10). The probe beams reflected from the transducer film are then directed to the detection system.

The configuration of the detection system is illustrated in Fig. 6. The probe beams were sequentially resolved by the LDMs, similar to the wavelength splitter, and stray light was eliminated from the resolved beams by the BP. Each probe beam that passed through its respective BP filter was detected using a photodetector (PD). The detected signals were then processed using a multi-channel lock-in amplifier, which measured the lock-in phase and amplitude signals synchronized with the modulation frequency.

3. Experimental section

3.1 Sample preparation

To inspect the speed of data acquisition and validity of the measurements, we tested the most basic structures as samples: Mo transducer/substrate; synthesized quartz glass (20 mm×15 mm×1 mm, ES grade, Tosoh Corporation), $SrTiO_3$(100) single crystal (10 mm × 10 mm × 0.5 mm, SHINKOSYA CO.,LTD), and c-plane sapphire (10 mm×10 mm×0.5 mm, Furuuchi Chemical Corporation) were used as substrates. Here, the $SrTiO_3$(100) single crystal and c-plane sapphire are referred to as STO and Al_2O_3, respectively. Table 1 lists the reported thermophysical properties for each substrate. To verify the thermophysical properties of those substrates, we employed a conventional TDTR apparatus to measure their thermal effusivity. The evaluated thermal effusivities were in agreement with the reported values within 6 % (See Supplemental Information, S1). A Mo transducer with an initial thickness of 100 nm was deposited on the substrates by means of dc magnetron sputtering using a Mo target (99.95% purity and 7.62 cm diameter). The sputtering chamber was evacuated to 10^{-4} Pa before the

deposition. The sputtering gas was a pure argon gas (99.9995 % purity) at a pressure of 1.0 Pa. The deposition was performed at a dc power of 100 W and the substrates were unheated. The thickness of the Mo layer was 94.2 nm as measured using a surface profiler (DektakXT).

3.2 Measurement conditions

The three types of substrates with Mo transducers were measured using HT-TDTR at room temperature. The pulse frequency was 78 MHz and the modulation frequency of the pump was 780 kHz. Incident optical powers of the probe beams in front of the sample were 2.0 mW for 900 nm, 2.2 mW for 850 nm, 2.6 mW for 830 nm, 1.8 mW for 815 nm, 2.1 mW for 790 nm, and 3.7 mW for 730 nm, respectively; while that of the pump beam, with a wavelength of 1064 nm, was 80 mW. The lock-in phase and amplitude of the reflected probe beams synchronized with the modulation frequency were measured using lock-in amplifiers with a time constant of 100 ms. These data were recorded for 300 s, and the thermal effusivity of the substrates was determined using curve fitting and machine-learning-based analyses. The detailed method is provided in the Supplemental Information.

3.3 Measurement data processing using machine learning

We have employed a machine learning (ML) model to predict the thermophysical properties from the experimental thermoreflectance signal of the HT-TDTR. Initially, we prepared a database containing 2,105 data sets, where one data set consists of interfacial thermal resistance between Mo and the substrate, thermal effusivity of the substrate, and phase signals derived by solving the one-dimensional heat transport problem reproducing the HT-TDTR measurement. Training data ranges of interfacial thermal resistance between Mo and substrate, and the thermal effusivity of substrate are from 0 m^2 K/W to 3.0×10^{-8} m^2 K/W and from 500 J/(m^2 $s^{0.5}$ K) to 16000 J/(m^2 $s^{0.5}$ K), respectively. We extracted a data set of these properties and phase signals from the database, corresponding to each delay time of the measurements. The data was then divided into training and test sets in a 1:1 ratio. Using the Python programming language and the Random Forest regressor from the scikit-learn library, we built the ML model to predict the interfacial thermal resistance between Mo and the substrate and thermal effusivity of substrate from phase signals at 5 delay times. As the hyperparameters, the number of jobs was configured to 10 and the number of estimators was set to 100. The other hyperparameters were left at their default values. The coefficient of determination, R^2 of the ML model accuracy reached approximately 0.88.

The offsets of experimental phase signals were corrected using the average of experimental phase signal at −120 ps for 300 s. Thermal effusivity and interfacial thermal resistance were predicted by the ML based on the experimental phase data at each delay time

sequentially averaged over the 300 s measurements. The uncertainty of ML prediction was evaluated by Monte Carlo simulation, in which 5000 sampling iterations were conducted to reproduce the normal distribution of phase signals at each delay time. The methodology for evaluating the uncertainty of the ML prediction is described in the supplemental information S3.

4. Results and discussion

4.1 HT-TDTR measurements

Figure 7 presents the lock-in amplitude V and phase θ of the TR signals for the samples obtained using the 830 nm probe, along with the histogram of θ during 300 s measurements. Here, θ represents the relative phase to that at 900 nm (delay time: −120 ps). In Figs. 7(a)–7(c), V exhibits no noticeable drift over time across all the samples and remains nearly constant. In Figs. 7(d)–7(f), θ does not exhibit significant variations over time, with fluctuations appearing within a certain noise range. The θ histograms in Figs. 7(g)–7(i) show that distribution of θ becomes broader in the order of quartz glass, STO, and Al_2O_3. This trend correlates with the lock-in amplitude, where a smaller amplitude results in greater phase noise.

Figure 8 shows the experimentally measured phase θ and the theoretical simulation for the Mo (94.2 nm)/glass, Mo (94.2 nm)/STO, and Mo (94.2 nm)/Al_2O_3 samples as a function of delay time. The experimental data points exhibit a general decreasing trend with increasing delay. The phase shift is most pronounced in the Al_2O_3 substrate, followed by STO and quartz glass, reflecting differences in thermal effusivity. The interfacial thermal resistance and thermal effusivity of the substrate are analyzed by solution of one-dimensional heat diffusion equation for a film/semi-infinite substrate geometry[14]. For the Mo layer, a volumetric specific heat of 2.53×10^{6} J/m^3 K and thermal diffusivity of 2.0×10^{-5} m^2/s are used for the analysis. The interfacial thermal resistances between Mo and quartz glass, and between Mo and Al_2O_3, are 1.0×10^{-9} m^2 K/W, whereas that between Mo and STO is even smaller at 1.0×10^{-10} m^2 K/W. Those interfacial thermal resistances are not quantitative due to insufficient sensitivity as shown in Fig.4. The thermal effusivity of STO is 5400 J/(m^2 s$^{0.5}$ K), and that of Al_2O_3 is 11500 J/(m^2 s$^{0.5}$ K), both of which agree with the reference values listed in Table 1 within 10 %. However, the thermal effusivity of quartz glass is 1830 J/(m^2 s$^{0.5}$ K), which deviates by approximately 25 % from the reported data. To investigate this discrepancy, the surface temperature of the sample is estimated using Equation 11 in Reference 4. Assuming a Mo reflectivity of 60 %, an amplitude of thermal absorption of 32 mW, a spot diameter of 25 μm, and a quartz glass thermal conductivity of 1.64 W/mK, the surface temperature is estimated to reach approximately 250 °C. The detailed calculation is provided in the Supplemental Information S2. At this temperature, the thermal effusivity of quartz glass is approximately 1990 J/(m^2 s$^{0.5}$ K), which is agreement with the experimentally obtained value within 10 % [17,18].

4.2. Machine learning analysis

To verify further accelerating the measurements, we adopted machine learning analysis to the HT-TDTR measurement data accumulated for 300 s [15,16]. Figure 9 shows thermal effusivity and interfacial thermal resistance predicted by the machine learning based on the experimental phase data at each delay time sequentially averaged over the 300 s. For the quartz glass substrate, which exhibited a sufficiently large amplitude of TR signal, the thermal effusivity remains nearly constant from the first data point taken at 0.1 s. In the case of STO, the thermal effusivity becomes stable within 1 s, although the standard deviation increases with the number of samples. In contrast, for Al_2O_3, which the amplitude of TR signal is smaller compared with the others, the thermal effusivity varies with time, showing a relatively large standard deviation of approximately ±4000 J/(m^2 $s^{0.5}$ K). After 300 seconds, thermal effusivity estimated by the machine learning model were approximately 1750 (J/m^2 $s^{0.5}$ K) for quartz glass, 4840 J/(m^2 $s^{0.5}$ K) for STO, and 10850 J/(m^2 $s^{0.5}$ K) for Al_2O_3. As shown in Fig. 9(b), the interfacial thermal resistance exhibits large fluctuations and standard deviation across all substrates throughout the measurement. In this study, the interfacial thermal resistance demonstrated limited sensitivity as shown in Fig.4 and could not be reliably determined using the machine learning. Thermal effusivity determined by fitting and predicted by machine learning are summarized in Fig. 9(c). In the case of quartz glass, similar thermal effusivities are obtained through machine learning and fitting. These values deviate by more than 10 % from the reference values, which, as mentioned earlier, is due to the temperature rise. In contrast, for STO and Al_2O_3, both methods agree within 5 %, and all results are within ±10 % of the reference. It is worth noting that thermal effusivity can be predicted quickly with reasonable accuracy from a limited number of delay points, provided that a sufficiently large amplitude of TR signal is available.

5. Conclusions

We developed an HT-TDTR system using a supercontinuum light source. The supercontinuum light was split into a pump beam and six probe beams with preset delays added to the probe beams, which enabled the simultaneous measurement of TR signals at different delay times. Using HT-TDTR, we measured the thermophysical properties of three samples: Mo (94.2 nm)/glass, Mo (94.2 nm)/STO, and Mo (94.2 nm)/Al_2O_3, each with a distinct thermal effusivity. The obtained thermal effusivity is in good agreement with the reference data. In addition, the machine learning model used for determining thermal effusivity enables accurate prediction from only a few data points in materials exhibiting large amplitude of TR signals. In the future, this technique will be applied to the characterization of the thermophysical properties

of multilayer samples, thermal conductivity mapping, and the measurement of temporal dynamics.

Declaration of Competing Interest

The authors declare that they have no known competing financial interests or personal relationships that could have appeared to influence the work reported in this paper.

Acknowledgements

This work was supported by JST-ERATO "Magnetic Thermal Management Materials Project" (No. JPMJER2201); JSPS KAKENHI (23K26057, 22H04953, 24K21593).

Data Availability Statement

The data that support the findings of this study are available from the corresponding authors upon reasonable request.

References

[1] M. Hatami, G.E.W. Bauer, Q. Zhang, and P.J. Kelly, Phys. Rev. Lett. **99**, 066603 (2007).

[2] H. Nakayama, B. Xu, S. Iwamoto, K. Yamamoto, R. Iguchi, A. Miura, T. Hirai, Y. Miura, Y. Sakuraba, J. Shiomi, and K. Uchida, Appl. Phys. Lett. **118**, 042409 (2021).

[3] R. Modak, Y. Sakuraba, T. Hirai, T. Yagi, H. Sepehri-Amin, W. Zhow, H. Masuda, T. Seki, K. Takanashi, T. Ohkubo, and K. Uchida, Sci. Technol. Adv. Mater. **23**, 772 (2022)

[4] D. G. Cahill, Rev. Sci. Instrum. **75**, 5119 (2004).

[5] A. J. Schmidt, X. Chen, and G. Chen, Rev. Sci. Instrum. **79**, 114902 (2008).

[6] J. Zhu, D. Tang, W. Wang, J. Liu, K.W. Holub, and R. Yang, J. Appl. Phys. **108**, 094315 (2010).

[7] S. Huxtable, D.G. Cahill, V. Fauconnier, J.O. White, and J.- C. Zhao, Nat. Mater. **3**, 298 (2004).

[8] J.-C. Zhao, X. Zheng, and D.G. Cahill, Scripta Materialia **66**, 935 (2012).

[9] J. Cho, M.D. Losego, H.G. Zhang, H. Kim, J. Zuo, I. Petrov, D.G. Cahill, and P.V. Braun, Nat Commun **5**, 4035 (2014).

[10] A.J. Schmidt, R. Cheaito, and M. Chiesa, Rev. Sci. Instrum. **80**, 094901 (2009).

[11] J.A. Malen, K. Baheti, T. Tong, Y. Zhao, J.A. Hudgings, and A. Majumdar, J. Heat Transfer **133**, 081601 (2011).

[12] J. Yang, C. Maragliano, and A.J. Schmidt, Rev. Sci. Instrum. **84**, 104904 (2013).

[13] E. Colavita, A. Franciosi, C. Mariani, and R. Rosei, Phys. Rev. B **27**, 4684 (1983).

[14] Y. Yamashita, Y. Aoki, T. Yagi, J. Jia, M. Kashiwagi, Y. Oguchi, N. Taketoshi, Yuzo

Shigesato, J. Appl. Phys. **130**, 085103 (2021)
[15] Y. Pang, P. Jiang, and R. Yang, J. Appl. Phys. **130**, 084901 (2021).
[16] Y. Mao, S. Zhou, W. Tang, M. Wu, H. Zhang, H. Sun, C. Yuan, J. Appl. Phys. **135**, 095102 (2024).
[17] Y. S. Touloukian, R. W. Powell, C. Y. Ho, and P. G. Klemens. "Thermophysical properties of matter - the TPRC data series. Volume 2. Thermal conductivity - nonmetallic solids." Plenum Press, New York, (1970).
[18] P. Richet, Y. Bottinga, L. Denielou, J. P. Petitet, C. Tequi Geochim Cosmochim Ac **46**, 2639 (1982)
[19] The thermal diffusivity and the specific heat of STO were measured by laser flash method and calorimetry, respectively. The thermal conductivity was calculated using these values and density.
[20] Y. S. Touloukian, R. W. Powell, C. Y. Ho, and P. G. Klemens. "Thermophysical properties of matter - the TPRC data series. Volume 5. Specific Heat-Nonmetallic Solids" Plenum Press, New York, (1970).

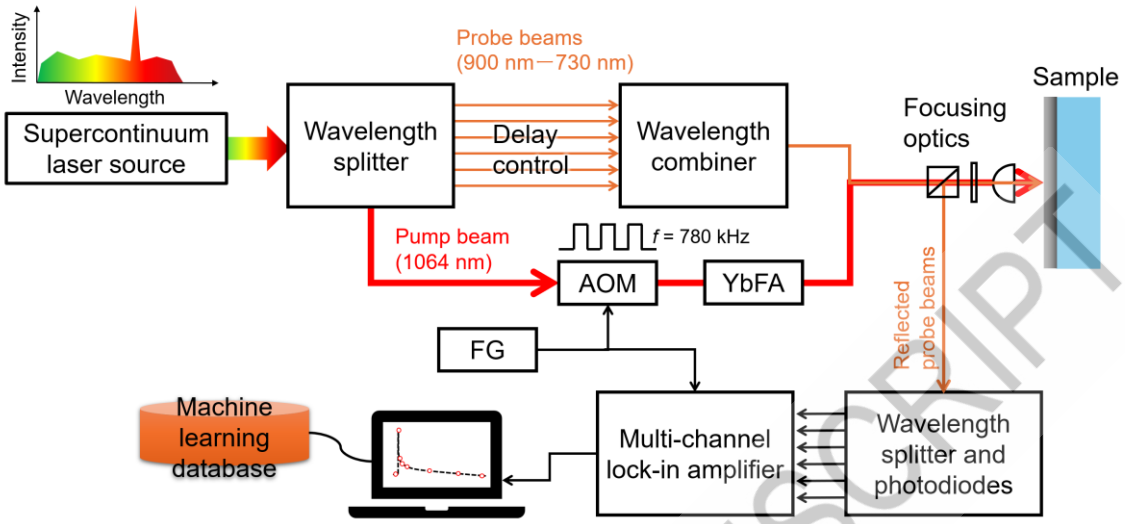

Figure 1 Overview of high-throughput time-domain thermoreflectance apparatus (FG: function generator. AOM: acousto-optic modulator, YbFA: ytterbium-doped fiber amplifier).

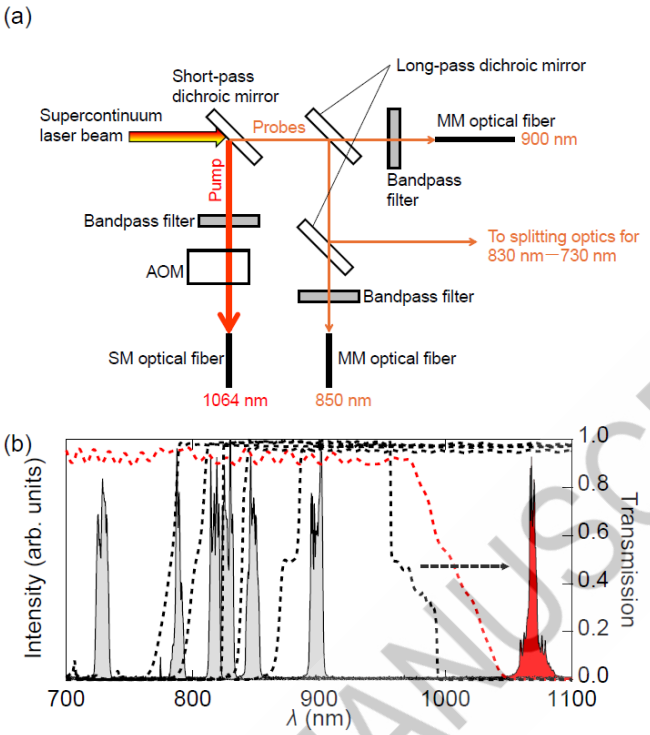

Figure 2 (a) Experimental configuration of the wavelength splitter system (SM: single-mode, MM: multi-mode). (b) The spectra of a pump (red) and six probes (gray) separated from the supercontinuum laser source. The dashed lines show transmission spectra of dichroic mirrors used for the wavelength splitter.

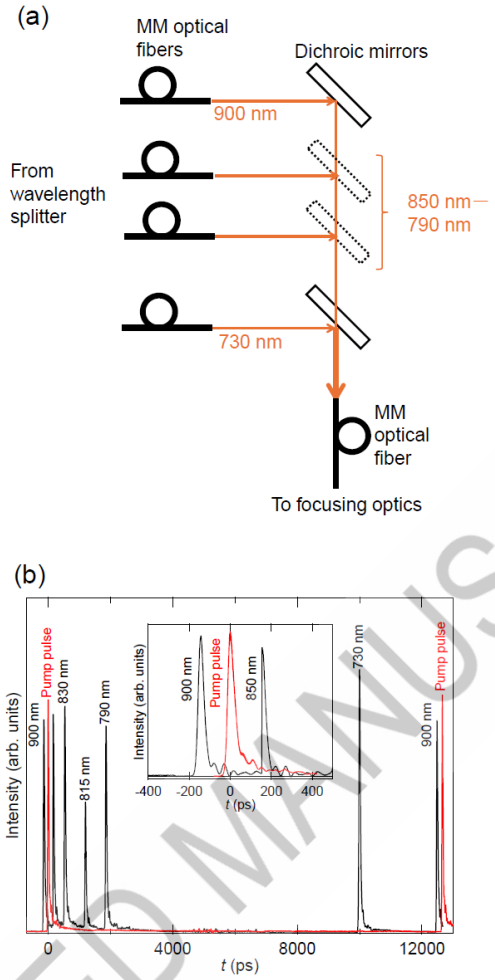

Figure 3 (a) Experimental configuration of the wavelength combiner system. (b) Pump pulse (red) and six probe pulses (black) observed by high-speed photodiode and oscilloscope.

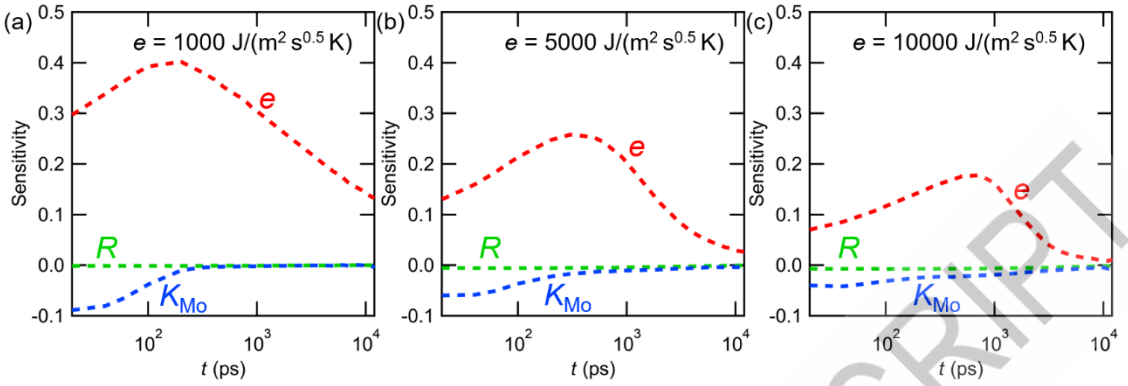

Figure 4 Sensitivity for phase: (a) for e = 1000 J/(m^2 s$^{0.5}$ K), (b) for e = 5000 J/(m^2 s$^{0.5}$ K), and (c) for e = 10000 J/(m^2 s$^{0.5}$ K). Volumetric heat capacity and thermal diffusivity of Mo are fixed at 2.53×10^6 J/(m^3 K) and thermal diffusivity of 2×10^{-5} m^2/s, respectively.

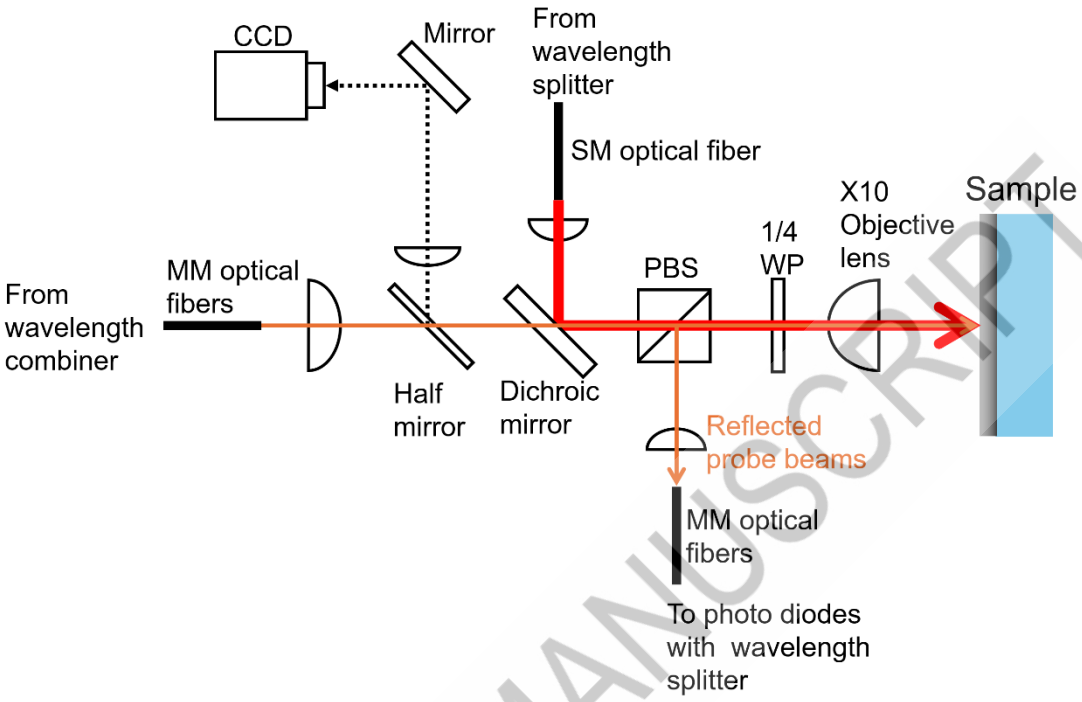

Figure 5 Experimental configuration of the focusing optics system. (PBS: polarizing beam splitter, WP: wave plate)

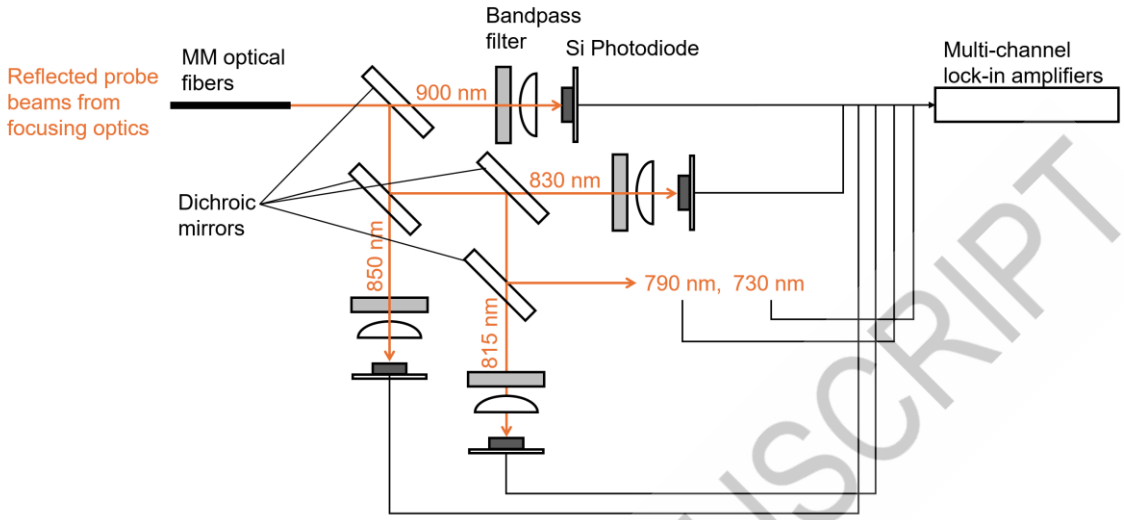

Figure 6 Experimental configuration of wavelength splitter, photodiodes, and multi-channel lock-in amplifiers.

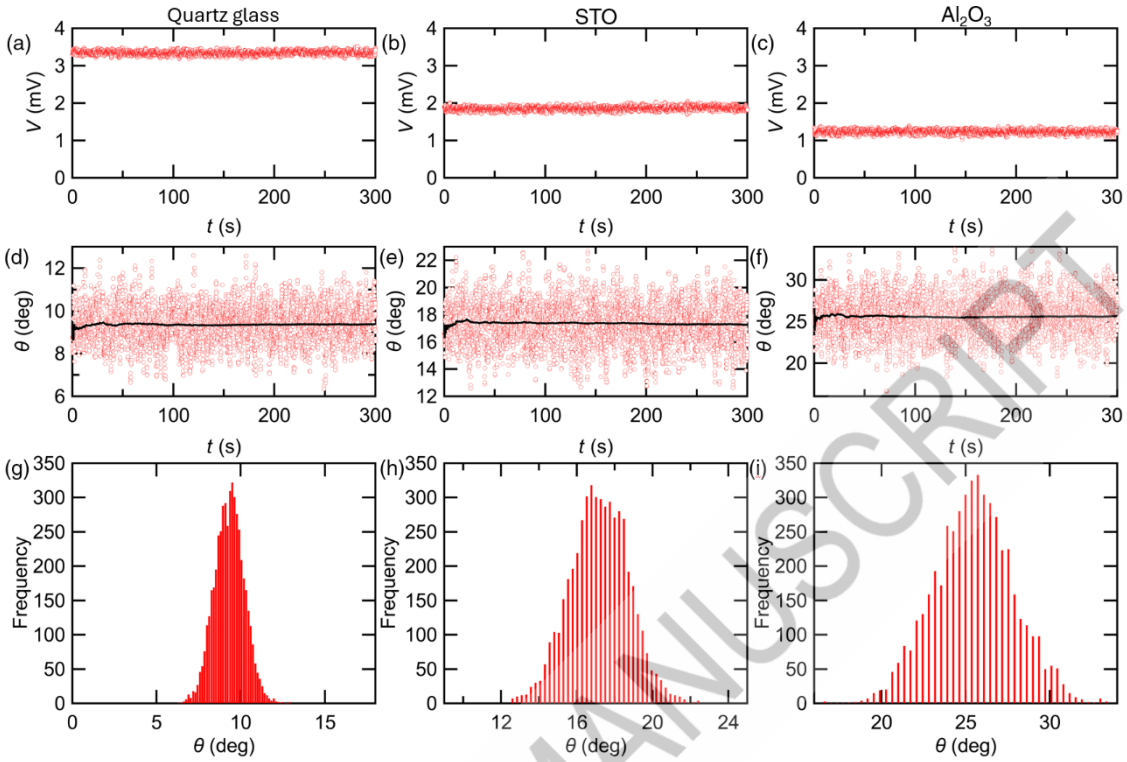

Figure 7 Time evolution and statistical distribution of measurement signals of the 830 nm probe light (523 ps of the delay time) for Mo (94.2 nm)/quartz glass, Mo (94.2 nm)/STO, and Mo (94.2 nm)/Al_2O_3 samples. (a–c) Time evolution of the amplitude V over 300 s for quartz glass, STO, and Al_2O_3 substrates, respectively. (d–f) Time evolution of the phase θ for each substrate, where red dots represent raw data, and the black line indicates the average up to t. (g–i) Histogram of phase θ distributions for each substrate for 300 s measurement.

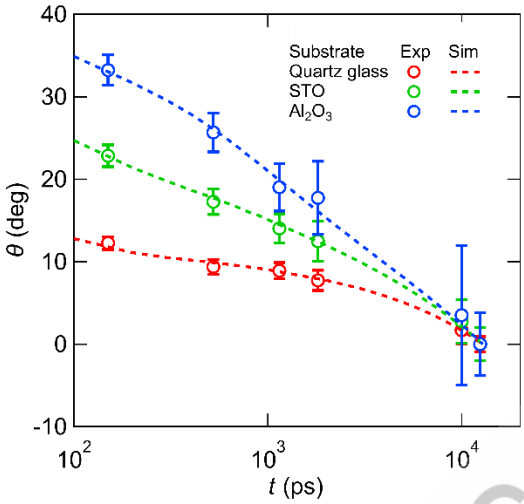

Figure 8 Delay time dependence of the lock-in phase of the thermoreflectance for Mo (94.2 nm)/quartz glass, Mo (94.2 nm)/STO, and Mo (94.2 nm)/Al_2O_3 samples. The white circles represent the experimental data, whereas the dotted lines denote the fitting curves.

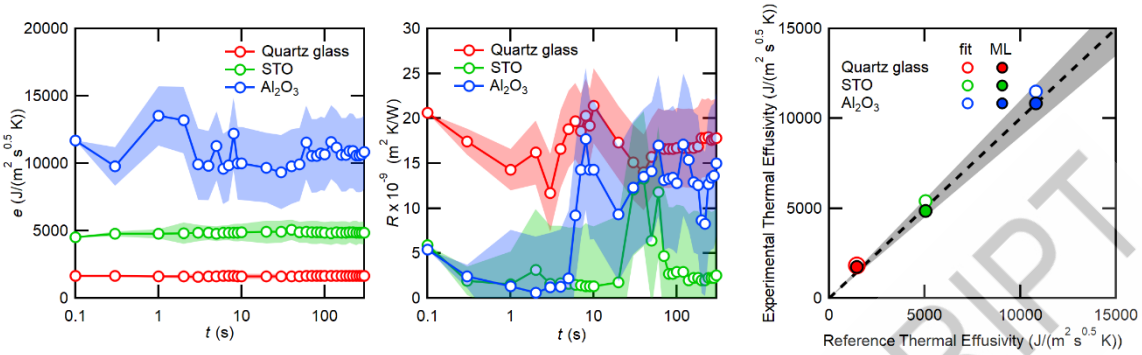

Figure 9. (a) Thermal effusivity and (b) Interfacial thermal resistance predicted by the machine learning based on the experimental phase data at each delay time sequentially averaged over the 300 s measurements. Color shade indicates the uncertainty of the ML prediction. (c) Comparison of reference and experimental thermal effusivity, where the experimental thermal effusivity includes determined by theoretical fitting (fit) and predicted by machine learning (ML). The dashed line indicates one-to-one match between reference and experimental values, and the shade area represents a ±10 % error range.

Table 1 Thermophysical properties of quartz glass, STO, and Al_2O_3

Substrate	Thermal effusivity $J/(m^2\ s^{0.5}\ K)$	Thermal diffusivity m^2/s	Thermal conductivity W/(m K)	Heat capacity J/(g K)	Reference
Quartz glass	1450	9.06×10^{-7}	1.38	0.69	[17][18]
STO	5040	3.43×10^{-6}	9.34	0.54	[19]
Al_2O_3	10800	1.24×10^{-5}	38	0.77	[17][20]

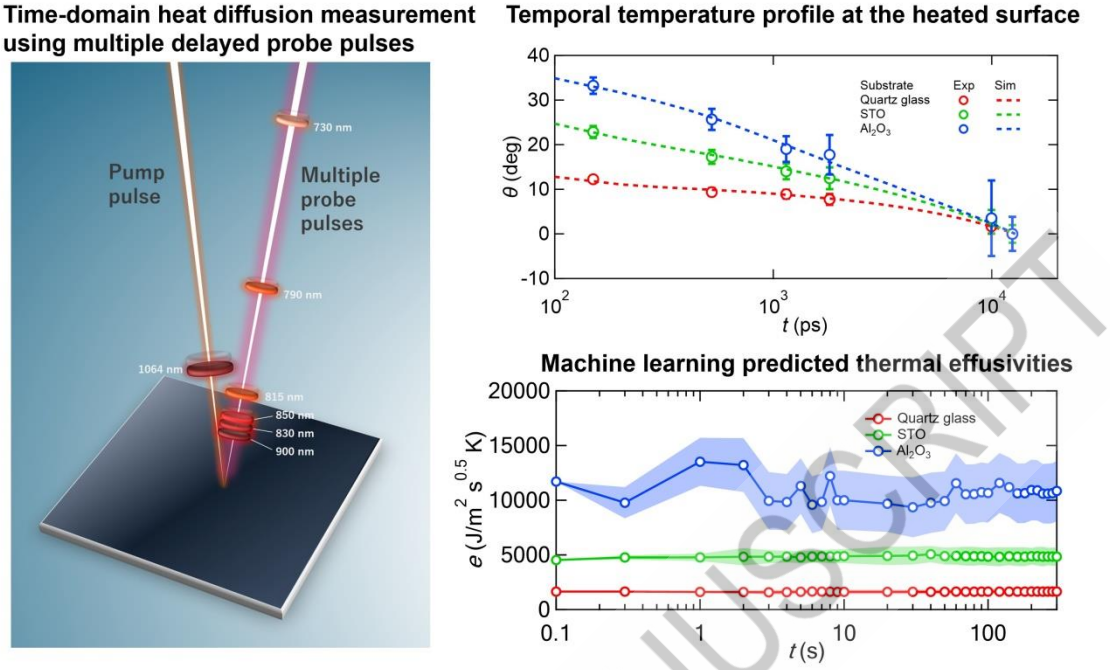

Graphical abstract

Statement of Novelty

Our high-throughput TDTR technique instantly captures picosecond-to-nanosecond thermal dynamics in materials, advancing the understanding of spatiotemporal heat transport and facilitating the development of next-generation thermal management materials.

Supplemental Information

Hiroto Arima, Yuichiro Yamashita, Takashi Yagi*

National Metrology Institute of Japan (NMIJ), National Institute of Advanced Industrial Science and Technology (AIST), Tsukuba, Ibaraki 305-8565, Japan

* t-yagi@aist.go.jp

S1 Examination of the thermal effusivity of the substrates

To verify the thermophysical properties of the substrates used in this study, we employed normal TDTR apparatus[s1-s3] to measure their thermal effusivity. The wavelength, the pulse duration, and the pulse frequency of the pump laser were 1550 nm, 0.5 ps, and 20 MHz, respectively. For the probe laser, the wavelength, the pulse duration, the pulse frequency, the average power, and the spot radius were 775 nm, 0.5 ps, 20 MHz, 1 mW, and 15 μm, respectively. The spot radius and the average power of the pump laser were set as 35 μm and 10 mW for the quartz glass, and 50 μm and 20 mW for the STO and Al_2O_3, respectively. The delay time was set as 1 ps step from -50 ps to 100 ps, 10 ps step from 100 ps to 1 ns, 100 ps step from 1 ns to 10 ns, and 1 ns step from 10 ns to 49 ns.

Measurement curves were shown in Fig.S1. For the fitting, we employed a volumetric specific heat of 2.53×10^6 J/m^3 K and thermal diffusivity of 2.0×10^{-5} m^2/s for the Mo transducer. Then, the thermal effusivity of the substrate and interfacial thermal resistance between the Mo transducer and the substrate were analyzed. In this figure, 10 % deviation of the thermal effusivity is shown along with best fit curves. The analyzed results are listed in Table S1. The evaluated thermal effusivities agree with the reported values within 6 %.

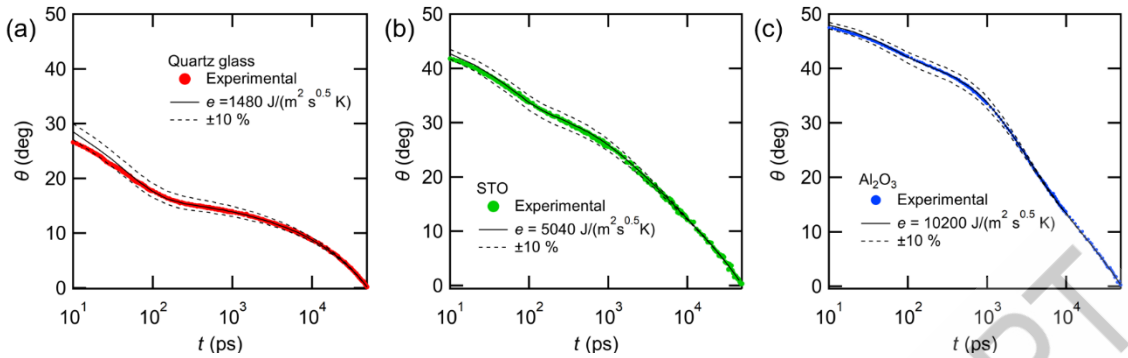

Fig. S1 Temporal lock-in phase of thermoreflectance for three kinds of substrates obtained by the conventional TDTR setup[s1-s3]

Table S1 Analyzed thermal effusivity and interfacial thermal resistance for three kinds of substrates.

Substrate	Reported thermal effusivity $J/(m^2\,s^{0.5}\,K)$	Evaluated thermal effusivity $J/(m^2\,s^{0.5}\,K)$	Evaluated interfacial thermal resistance $m^2\,K/W$
Quartz glass	1450[17,18]	1480	3.0×10^{-9}
STO	5040[19]	5040	3.0×10^{-9}
Al_2O_3	10800[17,20]	10200	3.3×10^{-9}

[s1] Y. Yamashita et al, *J. Appl. Phys.* 125, 035101 (2019)
[s2] T. Imaizumi et al, *Jpn. J. Appl. Phys.* **60** 038002 (2021)
[s3] H.Yagi et al, *Appl. Phys. Express* **16** 095503 (2023)

S2. Estimation of Surface Temperature of Mo (94.2 nm)/Quartz Glass Sample

The surface temperature increase (ΔT) of a Mo (94.2 nm)/quartz glass sample by heat pulse excitation in the low-frequency limit is estimated using the following equation [4]:

$$\Delta T = \frac{A_0}{2\sqrt{\pi} w_0 \Lambda}$$

Here, A_0 is the absorbed heat power, w_0 is the pump beam radius, and Λ is the thermal conductivity of quartz glass. In this study, the pump beam power at the sample surface is 80 mW. Figure S2 shows that the reflectance spectrum a Mo film measured by a spectroscopic

ellipsometer. As shown in Fig. S2, the reflectance of Mo at 1064 nm is approximately 60 %, giving A_0 = 32 mW. The beam radius w_0 is 25 μm, as noted in the main text, and the thermal conductivity of quartz glass is estimated to be approximately 1.64 W/(m K)[reference 17 at 520 K]. Substituting these values into the equation yields ΔT = 220 K. Assuming a room temperature of 300 K, the surface temperature of the Mo/quartz glass sample is estimated to reach approximately 520 K (247 °C). At this temperature, the thermal effusivity of quartz glass is approximately 1990 J/(m^2 s$^{0.5}$ K) [17].

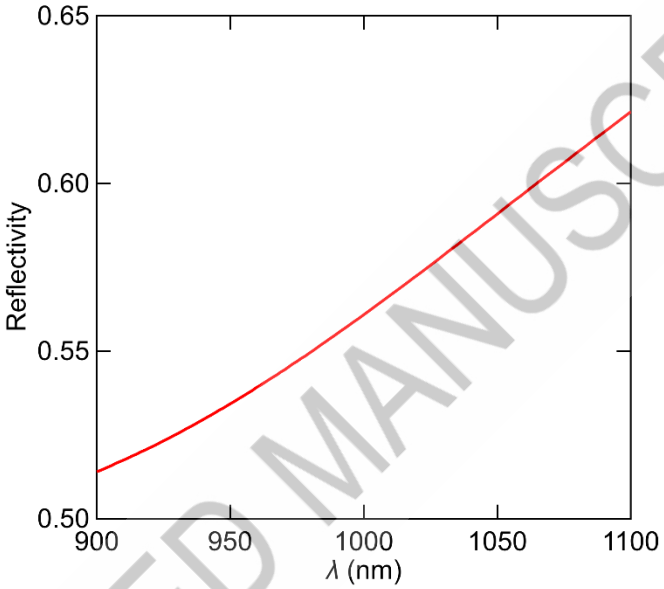

Fig.S2. Reflectance spectrum of Mo film measured by spectroscopic ellipsometer.

[4] D. G. Cahill, Rev. Sci. Instrum. **75**, 5119 (2004).

[17] Y. S. Touloukian, R. W. Powell, C. Y. Ho, and P. G. Klemens. "Thermophysical properties of matter - the TPRC data series. Volume 2. Thermal conductivity - nonmetallic solids." Plenum Press, New York, (1970).

S3 Uncertainty of ML prediction based on the experimental results

The uncertainty of ML prediction is evaluated based on a Monte Carlo simulation. The input parameters of ML are phase signals at the five delay times. We firstly calculated transition of standard deviations and means of experimental phase signals sequentially accumulated over 300 s. In the Monte Carlo simulation, we randomly sampled a series of phase signals from the obtained distribution at each delay time. Figures S3-S5 shows 5,000 times sampled phases by the Monte Carlo simulation from the experimental phase distribution accumulated up to 300 s. Generally, 5,000 times sampling is enough to reproduce normal distribution. Then, thermal effusivity of the substrate

and interfacial thermal resistance between the film and substrate were predicted using the ML model. We carried out the ML predictions at each sampling process. The standard deviation of 5,000 times predictions is the uncertainty including the experimental distribution and accuracy of the ML model.

In Figs.9(a) and (b), the color shades mean above uncertainty based on the standard deviations experimental phase signals sequentially accumulated from 0 s to certain measurement time.

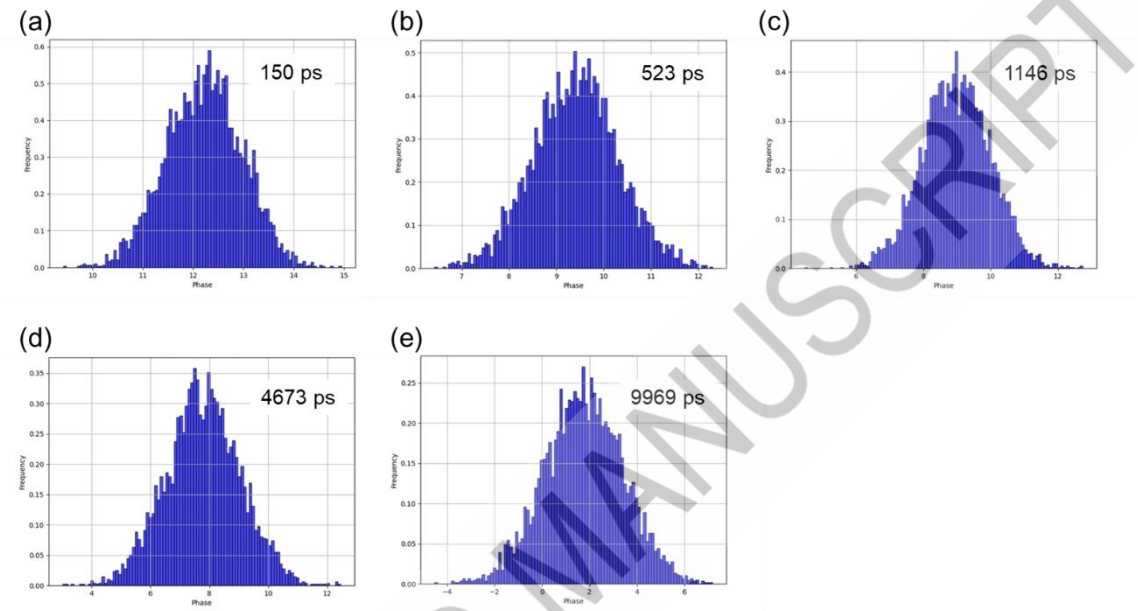

Fig. S3 Distributions of generated input parameter (phase signal) at measurement time of 300 s for each delay time to calculate the uncertainty of ML prediction in the case of quartz substrate: delay time of (a) 150 ps, (b) 523 ps, (c) 1146 ps, (d) 4673 ps, and (e) 9969 ps.

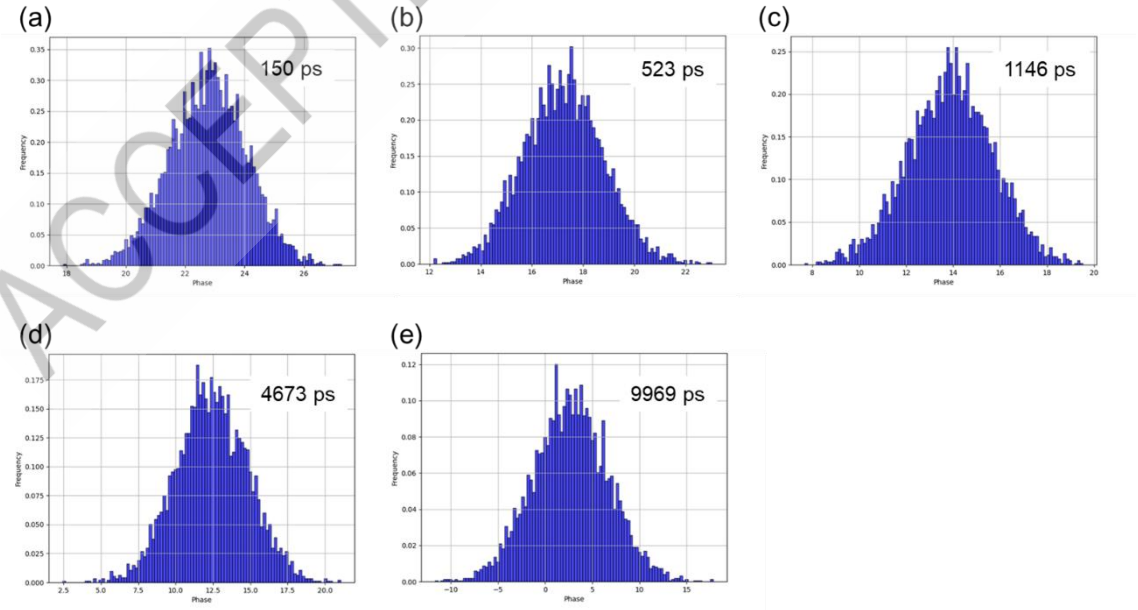

Fig. S4 Distributions of generated input parameter (phase signal) at measurement time of 300 s for

each delay time to calculate the uncertainty of ML prediction in the case of STO substrate: delay time of (a) 150 ps, (b) 523 ps, (c) 1146 ps, (d) 4673 ps, and (e) 9969 ps.

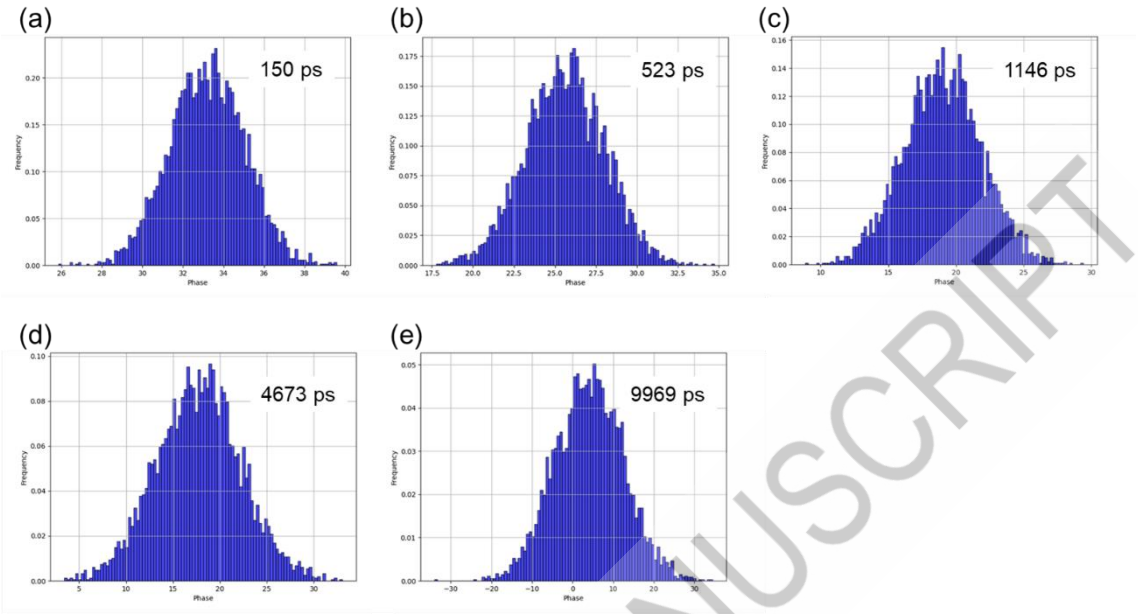

Fig. S5 Distributions of generated input parameter (phase signal) at measurement time of 300 s for each delay time to calculate the uncertainty of ML prediction in the case of Al_2O_3 substrate: delay time of (a) 150 ps, (b) 523 ps, (c) 1146 ps, (d) 4673 ps, and (e) 9969 ps.